Structure-from-Motion photogrammetry analysis of historical aerial photography: determining beach volumetric change over decadal scales

Rafael C. Carvalho [1*], David M. Kennedy [2,3], Yakufu Niyazi [1], Chloe Leach [2], Teresa M. Konlechner [2,3], Daniel Ierodiaconou [1]

[1] School of Life and Environmental Sciences, Deakin University, Warrnambool, Victoria 3280, Australia

[2] School of Geography, The University of Melbourne, Parkville, Victoria 3010, Australia

[3] National Centre for Coasts and Climate, The University of Melbourne, Parkville, Victoria 3010, Australia

*Corresponding author. E-mail: Cabralcar@deakin.edu.au; Phone: +61 3 55633052

Running Head: SFM ANALYSIS OF HISTORICAL BEACH CHANGE

R. C. CARVALHO *ET AL.*

This is the author manuscript accepted for publication and has undergone full peer review but has not been through the copyediting, typesetting, pagination and proofreading process, which may lead to differences between this version and the Version of Record. Please cite this article as doi: 10.1002/esp.4911

ABSTRACT: Historical aerial photographs are an invaluable tool in shoreline mapping and change detection in coastal landscapes. We evaluate the extent to which Structure-from-Motion (SfM) photogrammetric methods can be applied to quantify volumetric changes along sandy beaches, using archival imagery. We demonstrate the application of SfM-derived Digital Surface Models (DSMs) at East Beach and Lady Bay in southwest Victoria, Australia, using photographic datasets taken in 1969, 1977 and 1986, and compared them to Light Detection and Ranging-derived DSMs acquired at both sites in 2007. The SfM approaches resulted in two entire and two partial suitable DSMs out of six datasets. Good quality DSMs were spatially-continuous with a good spread of Ground Control Points (GCPs) near the beach at Lady Bay, whereas unsuitable DSMs were mostly restricted by poor distribution and number of GCPs in spatially-segmented areas of East Beach, due to limited overlapping of images, possible poor quality of GCPs and also the propagation of error in the derived point clouds. A volume of approximately 223,000 ± 72,000 m^3 was deposited at Lady Bay between 1969 and 2007, despite minimal erosion observed near the breakwater. The partially suitable dataset of East Beach indicated that beach erosion of at least 39 m^3/m occurred immediately to the east of the seawall after 1977. We also discuss the drawbacks and strengths of SfM approaches as benchmark of historical erosion assessments along sandy beaches.

KEYWORDS: SfM-MVS photogrammetry; Aerial photogrammetry; Volumetric comparison; Coastal change; Port Fairy; Warrnambool

Introduction

Photogrammetry has been long established data source in geosciences with analogue and more recently, digital aerial photography, contributing to making maps for more than a century (Birdseye, 1940). This aerial data source serves as a unique and extremely valuable historic archive of past landscape and built environment (Nebiker *et al.*, 2014). Aerial photogrammetry, the geometric reconstruction technique for obtaining 3-dimentional spatial information, relies on several issues including the quality of vertical aerial photography, flight plan, computation of photo-coordinates, aerial triangulation used to determined camera position and pose, and reconstruct scene geometry, resulting in a workflow that was often labour intensive and time-consuming (Baily *et al.*, 2003; Chandler, 1999; Fonstad *et al.*, 2013; Grip *et al.*, 2000; Schenk, 2005).

Structure-from-Motion (SfM) is a topographic survey technique that has recently emerged from traditional photogrammetry and advances in computer vision, offering potential to generate high accurate dense point clouds at different scales to restitute the three-dimensional geometry of objects or surfaces (Carrivick *et al.*, 2016; Fonstad *et al.*, 2013; James and Robson, 2012; Westoby *et al.*, 2012). SfM uses image matching algorithms that rely on multiscale image brightness and colour gradient between the object and its background to identify features present in multiple digital images regardless of changes in scale and viewpoints (Fonstad *et al.*, 2013). SfM photogrammetry works by calculating the geometry of the scene, camera location and orientation from the differential positions of multiple matched features that are tracked from image to image by using an interactive bundle adjustment procedure (Snavely, 2008).

Likewise in this paper, the SfM acronym is commonly referred as a simplified version of a much larger workflow that includes Multi-View Stereo (MVS) methods which usually refine 3D models to a finer resolution (Carrivick *et al.*, 2016). A typical SfM workflow summary presented by Carrivick et al. (2016) based on the works of others (e.g. Lowe, 2004; Snavely *et al.*, 2008; Triggs *et al.*, 1999) accounts for: i) features (keypoints) detection, ii) identifying correspondences between keypoints on different images, iii) removing geometrically inconsistent keypoints correspondences, iv) estimating 3D scene geometry, camera pose, and internal camera parameters (bundle adjustment), v) scaling and georeferencing the scene geometry, vi) optimising bundle adjustment parameters using ground control points (GCP), vii) clustering image sets for efficient processing, and viii) 3D scene reconstruction with MVS.

The computer vision techniques within SfM have allowed a qualitative improvement of the analysis by using much more of the information contained within the imagery to aid the orientation process, possibly unlocking large historical photogrammetric archives for morphologic analysis (Bakker and Lane, 2017). Recent examples of the application of SfM technique using historical aerial photographs have been published for river/floodplain systems (Bakker and Lane, 2017; Lane *et al.*, 2010), mountainous and hilly areas (Gomez *et al.*, 2015; Seccaroni *et al.*, 2018), volcanic islands (Gomez *et al.*, 2015; Ishiguro *et al.*, 2016), and glaciers (Mölg and Bolch, 2017). However, as far as the authors know, no study has applied the technique to understand morphodynamics of sandy beaches at decadal scale.

Here, we investigate whether it is possible to use SfM techniques to extract Digital Surface Models (DSMs) from historical aerial photogrammetric datasets taken in 1969 onwards, in order to quantify volumetric changes along sandy beaches in

southwest Victoria (Australia). DSMs from Lady Bay (LB) in Warrnambool and East Beach (EB) in Port Fairy were compared to airborne Light Detection and Ranging (LiDAR)-derived DSMs acquired at both sites in 2007. Analyses include evaluation of the accuracy of bundle adjustment processes and the suitability of historical DSMs, derived from SfM methods, as volumetric benchmarks for coastal erosion assessments at each site. We also discuss the drawbacks and the strengths of the SfM method in reconstructing past coastal geomorphic features and provide insights into the broader use of the technique in other sandy coastal systems.

Coastal setting

The study sites are located along the microtidal wave-dominated southwest coast of Victoria. LB, a 3.8-km long southern-facing embayed-beach from the breakwater (west) to the Hopkins River mouth (east), is located approximately 20 km to the east of EB, a 5.8-km long southeast-facing embayment that extends from the training walls of the Moyne River (southwest) to Reef Point (northeast) (Figure 1).

Most of Australia's southern shelf is subject to persistent high energy swells of above 3.5 m 30-50% of the time (Porter-Smith *et al.*, 2004) and significant wave heights of up to 8.7 m (Harris and Hughes, 2012). Both embayments can be considered leaky compartments due to sediment losses that occur due to longshore drift caused by predominantly southwesterly and westerly winds and waves propagating from west to east in the Southern Ocean. Wave conditions extracted from the CAWCR Wave Hindcast (Durrant *et al.*, 2013), for the 1986-2007 period, were characterised by a an average significant wave height of 1.62 m, period of 11.5 s and mean direction of 212.4º for EB, with comparable conditions for LB. Seasonal

variations are observed with higher wave heights (1.7 m), periods (12.2 s) and a more westerly wave approach (211^{o}) during Austral winters compared to lower wave heights (1.5 m), periods (10.5 s) and a more southerly wave approach (203^{o}), experienced during summer months, which for a short period of time can reverse the longshore current towards the west (Gill, 1984).

Insert Figure 1 here

The broad geology of the area consists of Miocene marine Port Campbell limestone capped with basalts of mostly Pleistocene age and fronted in the Warrnambool area by a large formation of Pleistocene aeolionite (Gill, 1967). The beach at LB is mostly composed of calcareous sand of different provenances. On the western side light grey coloured sand covers the surface, whereas light brown sand backed by Holocene dunes are observed along the northern and eastern shores (Gill, 1984) (Figure 1c). Shore platforms run out to the breakwater that shelters Warrnambool Harbour and end in Annabella Reef, whereas eroded aeolionites form a shore platform backed by a low cliff at the Hopkins River mouth (Gill, 1967). The seafloor of the bay is relatively flat, shallow and rocky, with a veneer of sand occupying depressions. On the eastern side of the bay, the Holocene dune and waves are much higher than near the breakwater. The beach forms a Low Tide Terrace (LTT)/Transverse Bar and Rip (TBR) at the Surf Life Saving Club (SLSC), with rips first occurring nearby and increasing in size and intensity towards Point Ritchie (Short, 1996).

LB was subject to rapid sediment accretion and progradation of over 300 m on its western side, and some erosion along its northern shore, following a succession

of coastal management decisions which included the construction of the viaduct and the breakwater in the late 1800's (Gill, 1984). More recently, seasonal analysis of four multibeam echosounder surveys conducted by Schimel et al. (2015) revealed that the seafloor of the bay near the breakwater experienced large sediment transfer (mostly erosion) between July and November 2013, whereas Ierodiaconou et al. (2016) calculated a volumetric loss of approximately 7,260 m^3 (average of 12.2 m^3/m) from the beachface and consequent retreat of the foredune along 550 m of shoreline near the breakwater following a major southwesterly storm event that happened in June 2014.

Basalts from the Mount Rouse lava flow form the coastline to the south and southwest of EB, and also outcrop on the coast at Reef Point (Gill, 1967; Ollier, 1985) (Figure 1b). Holocene calcareous sands form the present-day curved beach and grassy dune of EB, which increases in height and width towards the northeast. The beach is backed by dune calcarenite ridges that were formed approximately 80,000 years ago, when the sea level reached four meters higher than present (Bird, 1993). Wave height is lower in the southwest, near the Moyne River entrance than towards Reef Point. The beach is fronted by a single continuous inner attached bar in the southern corner until the proximity of the SLSC, which has a LTT/TBR morphology (Short, 1996). An outer bar and a series of rips are observed further to the north as a result of changing wave conditions.

Port Fairy was an important trade and whaling port during colonial times. Training walls initially built at the entrance of the Moyne River in late 1800's, and the closing of the southwest passage a few decades later, led to erosion issues at EB and accumulation of sand updrift (Flocard *et al.*, 2013; WBM, 2007) (Figure 1b). Sand dredged to maintain navigation into the river was placed in the Puddney

Grounds until the early 1990s and more recently near the southern end of EB, where an old basalt breakwater was built (1910's) to protect the shoreline. Along the southeastern end of EB a 2.2 km boulder seawall was constructed in the 1950's and several 30 m timber groynes in the 1970's, to protect the shoreline from reoccurring erosion. Engineering works have reinforced and redesigned the seawall and gradually extended its northern limit in the past three decades (Flocard *et al.*, 2013). A past landfill site was created in the 1970's along the coastal dunes backing the shoreline about 1.4 km from the end of the seawall. Since then, beach recession has exposed contaminant and debris, and a seawall to prevent further erosion was constructed in 2015 (Miles, 2019).

The shoreline to the east of Port Fairy is characterised by Holocene sand ridges up to 7.5 m high until Tower Hill, where the coastline changes to a southeastward orientation. 30-m high dunes underlain by Late Pleistocene dune calcarenite, which eventually outcrops as low cliffs and shore platforms forms the coastline from Tower Hill to the mouth of Merri River in Warrnambool (Bird, 1993; Gill, 1967).

Methods

SfM was applied to historical aerial photographs acquired specifically for traditional photogrammetric approaches over LB in Warrnambool and EB in Port Fairy. A widely-used commercially-available software package (Pix4Dmapper) was used to assist bundle adjustment and georeferencing of historical DSMs and orthomosaics. Airborne LiDAR data were processed and used in two different ways in this study. Firstly, to extract bare ground data used as ground control points (GCPs) and as independent points used in accuracy assessments of SfM-derived

DSMs. Secondly, to generate LiDAR-derived DSMs for volumetric comparison against the SfM-derived DSMs.

LiDAR data

Airborne LiDAR data surveys carried out between 15 Aug and 17 Sep 2007 with an ALTM- Leica ALS50 sensor, as part of the Future Coast Program, were provided by the Victorian Department of Environment, Land, Water and Planning (DELWP). The LiDAR sensor calculated XYZ and intensity data for first and last returns by bouncing a pulse from the aircraft to the surface, at an average point density of 1.9 pts/m^2, footprint size of 0.6 m and stored in LAS 1.2 Classification Level 2 format. Posterior classification of the data into a higher accuracy product (ICSM Level 3) organized in 2 x 2 km tiles, were provided by the contractors. Horizontal and vertical accuracies (RMSE 68% Conf.) of 0.35 m and 0.1 m, respectively, were reported in the metadata.

The provided LiDAR LAS files were converted to bare ground (class 2) multipoint feature classes in ArcMap 10.7.1 with an average point spacing of 1 m, based on the specifications defined by the American Society of Remote Sensing (ASPRS). Multipoints were converted to singlepart feature classes, and elevation information (Z) was added to individual features. Points from locations where vertical change was believed to be minimal such as road intersections and driveways, were selected as GCPs to georeference historical DSMs and orthomosaics. Extra independent points were also retrieved and used in accuracy assessments of SfM-derived DSMs (Figure 2).

A LiDAR-derived DSM was created for each study site by processing the individual LAS files into multipoints (average point spacing of 1 m) using classes 2 (bare ground), 3 (low vegetation), 4 (medium vegetation), 5 (high vegetation) and 6 (building), and then into singlepart feature classes. The processing using these specific classes was needed in order to generate DSMs based on pulse returns that would represent the top of vegetation and buildings that could be compared to SfM-derived DSMs. Once processed, a Triangular Irregular Network (TIN) was created for each embayment using two tiles for LB and four tiles for EB. Subsequently, the TINs were converted to 0.2 m pixel raster datasets resulting in 2007 LiDAR-derived DSMs used in comparison to SfM-derived DSMs.

Insert Figure 2 here

Historical aerial photographs

Scanned analogue aerial photographs were provided by DELWP in high resolution (approximately 250 Mb/photo) digital format (.tiff). We opted for analysing images acquired at 1:15,000 or higher scale in order to obtain high spatial resolution on the ground and to avoid too much scale variation between datasets. Selected photographs were acquired in 1969, 1977 and 1986 for both EB and LB at image scales of 1:10,000 and 1:12,500. Specific images from each flight run were selected for reconstruction of DSM according to photograph characteristics in Table I.

Insert Table I here

241 DSMs and orthomosaics

242

243 Prior to SfM initial processing, the black frame around each photograph was
244 removed using a batch cropping process in Adobe Photoshop (Figure 2). Preliminary
245 DSMs and orthomosaics were generated for each dataset using arbitrary
246 coordinates (no scale, orientation and absolute position information), as scanned
247 photographs had no geolocation. The SfM initial processing used full keypoints
248 image scale and the point cloud densification was created with half image size,
249 optimal point density and a minimum number of 3 matches.

250 The arbitrary DSMs were generated using noise and sharp surface smoothing
251 filtering, and Inverse Distance Weighting interpolation. The DSMs and orthomosaics
252 allowed a preliminary understanding of the spatial extent of each dataset and a
253 visual identification of undisturbed parts of the landscape from where GCP locations
254 could be identified in order to guarantee a good spread of control points throughout
255 each DSM. Owing to the difficulty in identifying points of minimum change since
256 1969 in parts of the models, extra inland photographs were added extending the
257 modelled areas and allowing a better distribution of GCPs to enable a more accurate
258 reconstruction (Bakker and Lane, 2017).

259 Georeferenced point clouds were generated by re-processing the arbitrary
260 products with GCPs as a posteriori (Bakker and Lane, 2017; Nebiker *et al.*, 2014)
261 with 0.5 m accuracy in X, Y and Z domains. This was performed using the same
262 initial processing and point cloud densification configurations. Final models used a
263 minimum of 15 GCPs each according to Table II, and their spatial distribution can be
264 found in Figure 3.

265

Insert Table II here

Point clouds were manually cleaned to remove common data spikes from SfM approaches. Artefacts were most predominant over water and homogeneous low texture areas such as roads and parts of the beach. Final DSMs and orthomosaics were created using the same initial configurations and 3D texture meshes were generated using medium resolution for fly through visualisations.

Insert Figure 3 here

Volumetric comparison

DEMs of Differences (DoDs) were computed using ArcMap via the subtraction of the historical DSMs from the 2007 LiDAR-derived DSM at each site. Subtraction of the elevation values provided information at pixel level (0.2 x 0.2 m). A positive value indicates whether the location represented by the pixel has accreted, whereas a negative value indicates an area of erosion.

Volumetric comparisons were restricted to a 30-m wide area along the beach that were common to all datasets and calculated above 0 m AHD (Australian Height Datum, equivalent to Mean Sea Level). This masked area covered mostly the beachface in order to avoid urbanized and vegetated areas that were subjected to change.

Volumetric analysis were limited to the DoD pixels displaying an absolute value larger than the limit of detection (LoD), which accounted for areas that experienced little change to be removed from the calculations (Ierodiaconou *et al.*, 2016). A LoD

was used for each DoD based on the standard deviation of RMSEs reported in Table III as an estimation of its inherent uncertainty. The LoD threshold is a common approach to remove from volumetric calculations, the areas which display a small difference in elevation due to the uncertainty in the DSMs (Wheaton *et al.*, 2010). Volumetric uncertainty was then calculated using the area experiencing change (number of pixels x pixel area) multiplied the LoD.

While the volumetric analysis over the entire beachface provided a general assessment of sediment change on each site, an extra analysis was conducted using 100-m spaced shore-perpendicular transects to gain further spatial insight on a more localised level. For that, we defined a 1-m wide x 30-m long polygon at each transect and calculated volume of sand for each DSM, thereby providing an estimate of change in volume per metre length of beach (m^3/m) for each site.

Shoreline analysis

Shoreline analysis was carried out in DSAS v5.0 (Himmelstoss *et al.*, 2018). The edge of coastal vegetation was digitised from the georeferenced orthomosaics and aerial photographs taken in 2007 during the LiDAR survey. The vegetation line was used as the shoreline for all analysed datasets. Net shoreline movement (NSM), shoreline change envelope (SCE) and linear regression rate (LRR) were computed as change statistics using 10-m spaced shore-perpendicular cast transects.

Results

SfM and model accuracy

Ground Sampling Distance (GSD) varied from 15.4 to 18.6 cm reflecting different flight altitude and camera parameters for each individual model (Table II). The best and worst georeferencing of all models were obtained by the LB 1986 and EB 1969 models, as indicated by their respective RMSE of 0.52 m and 0.98 m.

A minimum of 53,155 keypoints per image in EB 1977 was the worst result obtained for all models (range of 53,155 - 86,025 keypoints per image), indicating that all the historical timeseries had enough visual content to be processed. A fast and robust camera optimisation was only obtained for EB 1969 (0.6%). All other SfM models performed beyond software recommendation (5%). These results, however, should not be over interpreted as the analogue camera parameters were not correctly defined or found in Pix4D database. A minimum of 13,789 average matches per calibrated images were obtained for all datasets indicating that results are likely to be of high quality in the calibrated areas.

The spatial extent of SfM models varied from approximately 5 km^2 (LB 1986) to 13.8 km^2 (EB 1969) as a function of the number of photos, the flight scale and overlap of images (Table II and Figure 3). Only LB 1969 and LB 1979 models covered the whole beach, whereas no model covered the entire length of EB. EB 1977, EB 1986, and LB 1986 were segmented as a function of the poor overlapping (minimum of 3 photos required) of images continuously throughout the area, and therefore parts of these beaches were not reconstructed in the subsequent models.

Accuracy assessment of DSMs based on the coefficient of determination (R^2) showed a very strong relationship between the independent LiDAR-derived elevation points and the elevation extracted from the SfM-derived DSMs at localities identified as unlikely to change. A stronger correlation was observed for all LB models (0.99)

than for the EB models (0.84 to 0.96) and the histograms of error distribution show a wider spread and stronger asymmetries in EB 1969 and EB 1986 than the other models (Table III; Figure 3).

RMSE of independent points varied from 0.5 to 0.63 m for LB, and 0.62 to 1 m for EB, depending on the year. Mean errors (ME) of -0.03 to -0.46 m with standard deviation errors (SDE) of less than 0.6 m were obtained for LB models, whereas ME of -0.57 to 0.62 m and SDE of up to 0.92 were observed in EB models. Mean absolute errors (MAE) varied from 0.38 m (LB 1977) to 0.7 m (EB 1969) (Table III).

Insert Table III here

Elevation difference between 2007 LiDAR and points retrieved from individual DSMs are shown in Figure 3. Elevation difference near the coast are much lower for LB models than for the EB ones, suggesting that SfM models were more accurate for LB than for EB. Absolute differences greater than 1.5 m are observed in all EB models, as evidenced by the red dots in Figure 3, which indicate that elevations in the 1969 and 1977 models are higher than LiDAR, and the dark blue dots, which show that elevations in the 1986 model are lower than LiDAR.

Historical DSM comparisons

Figure 4 shows the coastal area of all SfM- and LiDAR-derived DSMs encompassing only the beach and the adjacent backdune for quick comparison. As expected from the accuracy results, elevations in SfM-derived DSMs for LB are much closer to 2007 LiDAR DSMs than for EB. Elevations were very similar for all

LB models, and a slightly increase due to urban development and tree growth is observed towards both west and east side of the models over time. Conversely, EB 1969 seems to have higher elevations than the EB 2007, whereas most of EB 1986 seems lower than the LiDAR DSM. The EB 1977 DSM seems to be the only comparable to the LiDAR DSM, especially the southwest part of the embayment.

One of the greatest advantages of SfM datasets is the ability of providing insights into coastal dynamics via unlimited perspectives of the landscape, as exemplified in Figure 5. An oblique view of a section of the shoreline near the SLSC at LB in 1969, 1977 and 1986 (Figure 5a, b and c, respectively), allows to understand how the coastal vegetation evolved (fluctuation of the beach profile at a specific transect in all three datasets can be seen in Figure 5d). At EB, a section of the coast in 1977 (Figure 5e) and 1986 (Figure 5f) can be used to understand when the seawall expansion occurred and the subsequent implications this had on the evolution of the beach.

Insert Figure 4 here

Insert Figure 5 here

Volumetric and shoreline comparisons

Visual inspection of DoDs at places where changes over time were not expected, such as along roads, undeveloped parcels of land and grassy areas

provided further insights into the quality of DSMs (Figures 6 and 7). At these places, DoDs should not vary considerably.

DODs clearly show that the segmented eastern half of LB 1986 (Figure 6), as well as both EB 1969 and EB 1986 DSMs, and the three segmented northeastern and the southwestern areas in EB 1977 (Figure 7), are vertically offset when subtracted from the 2007 LiDAR data. Therefore, volumetric analysis will be limited to LB 1969, LB 1977 and the suitable areas within LB 1986 and EB 1977 only.

Insert Figure 6 here

Insert Figure 7 here

Volumetric comparison conducted within a 30-m wide area along the entire beach (3.8 km of coastline) of LB shows an accretion of approximately 223,190 ± 71,840 m^3 (above 0 m AHD) between 1969 and 2007, and 199,340 ± 55,800 m^3 between 1977 and 2007. A calculated accretion of 48,140 ± 28,360 m^3 occurred between 1986 and 2007 for the western half of the embayment only (along approximately 1.8 km of coastline) (Figure 6). The general pattern is very similar for all three DoDs, as light erosion occurred along the first 400 m (taking the breakwater as the starting point), and accretion occurring further to the east. A maximum volumetric loss of approximately 15 m^3/m of beach occurred in the first 400 m between 1966 and 2007, whereas the coastline accreted at a maximum rate of approximately 80 m^3/m about 200 m to the west of the SLSC as indicated by the 2007-1977 volumetric change (Figure 6d).

At EB, the 2007-1977 DoD (Figure 7b) showed a slight decrease in volume of approximately 3,730 m^3 above 0 m AHD through the restricted analysed area from the SLSC to the landfill site, with two distinct areas segmented where the seawall ends. To the northeast of the seawall, a decrease in volume of approximately 13,000 ± 9,670 m^3 (along approximately 1.3 km of coastline) occurred, whereas from the end of the seawall to the SLSC (approximately 1.1 km of coastline), an accretion of approximately 9,250 ± 6,620 m^3 was observed. A loss of approximately 39 m^3/m occurred immediately to the east of the seawall (Figure 7d).

Shoreline analysis at LB (Figure 8) shows a positive LRR (0.7 m/yr maximum) in most of the embayment and a minor negative LRR (0.2 m/yr maximum) near the breakwater (Figure 8b), between 1969 and 2007. During this period, a maximum shoreline progradation of 27 m occurred, as determined by SCE (Figure 8c). NSM indicates that most of the progradation experienced to the east of the SLSC occurred before 1986, and after that retreat happened (Figures 8d, e and f).

Insert Figure 8 here

Shoreline analysis at EB (Figure 9) shows a strong negative LRR of up to 0.5 m/yr in the first 500 m to the northeast of the seawall and a positive LRR observed further to the east (Figure 9b), between 1969 and 2007. During this period, a maximum shoreline movement of 17.2 m occurred to the northeast of the seawall, as determined by SCE (Figure 9c). The distance between the 1969, 1977, 1986 and 2007 shorelines indicates that the experienced retreat near the seawall occurred continuously through time, whereas at the landfill site considerable progradation of up to 9 m occurred prior to the retreat experienced after 1977 (Figures 9d, e and f).

Insert Figure 9 here

Discussion

This study has demonstrated that SfM approaches can be used to approximately quantify volumetric changes along sandy beaches using historical photogrammetric archives, acting as benchmarks for coastal erosion studies in Victoria and elsewhere. We were successful in calculating beachface volume for entire (LB 1969 and LB 1977) and partial (LB 1986 and EB 1986) datasets. The approach also generates seamless photomosaics, which can be used in traditional shoreline analysis, and allows detailed perspectives to investigate coastal processes based on unlimited defined angles and elevation views.

Volumetric and geomorphic beach change

The results presented for LB suggest that the western side may have reached an equilibrium after the rapid accretion following the construction of the viaduct and breakwater in the late 1800's (Gill, 1984). Indeed, this idea corroborates with bathymetric findings which show that a volume of approximately 7,000 m^3 was eroded from the subaqueous part of the beach between July and November 2013 (Schimel *et al.*, 2015). However, there is plenty of evidence that suggests that the western side of LB is still infilling.

Firstly, the volumetric calculations by Schimel et al. (2015) were conducted during the erosive Austral winter and spring, excluding the recovery part of the short-

term seasonal fluctuation (Thom and Hall, 1991). Secondly, it appear that fine sediments deposited to the south of the breakwater by longshore drift (Schimel *et al.*, 2015), can bypass the breakwater and accumulate in the leeward side (Water Technology, 2012). In fact, the ongoing deposition of sediments into the lee of the breakwater has led to the dredging of the harbour several times in the past decades, which may explain why the adjacent shoreline is eroding while the nearshore is still naturally accreting. Approximately 45,000 m^3 of sediments have been dredged from the area and disposed towards the middle of the bay in 2009 (Neal, 2012), whereas in other times dredged material has also been taking out of the system to retention ponds behind the foredune (WCC, 2019).

The general overlapping of the three cross-section lines in the first 500 m of LB (Figure 6d) suggests that the erosion occurred after 1986. This recent erosional pattern in the 500 m close to the breakwater was also observed by Ierodiaconou et al. (2016) following a southwesterly storm in 2014, which removed a maximum of 28 m^3/m from the area. The fact that the decadal maximum volumetric cut was about half of the calculated for the storm event can be attributed to the beach nourishment that occurred during the dredging of the Warrnambool harbour in 2001 and 2005, which possibly added an extra 46,000 m^3 to the shoreline (GHD, 2009), and also to the long time needed for these environments to recover from single events as observed in other sandy beaches (McLean and Shen, 2006; Turner *et al.*, 2016). Based on the experienced volumetric losses in recent decades, and the regular need for dredging the harbour, we suggest that management of this area should consider the possibility of further shoreline erosion driving the retreat of the foredune and possibly the loss of beach accesses and the coastal track behind it.

Further to the west of the initial 500 m until the SLSC, the accretion pattern was evident by all beach cross-section lines (Figure 6d) indicating that overall, this stretch of coast gained sediments from 1969 to 2007. However, it is also possible to conclude that this part of the coastline lost volume after 1986, as suggested by lower volumetric gain experienced between the 1986 and 2007 (red line) than over the other two periods (blue and orange lines). In fact, most of the volume gained along LB occurred between 1969 and 1977 as indicated by the blue line (Figure 6d) and the NSM maps in Figures 8d, e and f. Furthermore, the shoreline retreat experienced to the east of the SLSC between 1986 and 2007 (Figure 8e) also suggests that volumetric losses extended to the east of LB.

A much more limited volumetric calculation could be achieved at EB than at LB, as only a partial dataset was deemed suitable of analysis, and therefore the pattern of volumetric change over the 1977-2007 period could not be compared to any other period. The 1.3 km stretch of coastline starting at the end of the seawall until the western side of the landfill has experienced significant erosion and shoreline retreat (Figures 7d and 9) as a whole, with severe magnitude in the first 300 m since 1977, as expected to have happened on the downdrift side of most seawalls due to scouring (Kraus and McDougal, 1996; Plant and Griggs, 1992).

A close look into the zoomed-in area of Figure 7b reveals that the reported losses of approximately 13,000 ± 9,670 m^3 can be considered conservative volumes as severe erosion was observed outside the 30-m wide area used in volumetric calculations. Shoreline analysis along this stretch of coast (Figure 9) indicates that recession has occurred from 1977 to 2007, with recession rates similar to the ones calculated by Flocard et al. (2013) for the 1948-2010 period. This interpretation is also supported by a recent analysis of the dune toe vegetation to the east of the

seawall which found a decline in early-colonising species associated to higher rates of erosion (Konlechner *et al.*, 2019).

The zoomed-in Figure 7b also suggests that the volume increase of approximately 9,250 ± 6,620 m^3 to the southwest of the seawall end were driven by improvements to the structure and not volumetric changes in sand, and therefore must be treated with caution. Because of the seawall, shoreline analysis could not shed light into volumetric calculations along this part of EB.

The erosion experienced over the past decades at EB has been significantly intensified by management actions more than 100 years ago, which increased the trapping of sediments around Griffiths Island and consequently reduced the natural longshore drift of sediments to the east (Figure 1). The beach near the lighthouse, for instance, prograded a distance of 100 m between 1925 and 1992 (WBM, 2007), and is still accreting (Aurecon, 2010).

Qualitative comparison of LiDAR and elevations from the nautical charts of the colonial period by Barrow (1854) and Stanley (1870), indicates a massive volumetric deposition updrift around Griffiths Island. Previous attempts to calculate the volume accumulated there and lost from the longshore system varied from 500,000 m^3 to 700,000 m^3 since the construction of the training walls and the closing of the southwest passage (Flocard *et al.*, 2013; WBM, 2007). This is equivalent to an average of 86 to 120 m^3/m lost from EB, a volume 2 - 3 times greater than the maximum volumetric loss (39 m^3/m) calculated between 1977 and 2007 (Figure 7d). The losses during the 30-year period were probably reduced because of the management decision taken in the 1990s to pump dredged sand from the Moyne River onto the southern end of EB (WBM, 2007).

Future management actions for both embayments will also have to consider a more acidic Southern Ocean (McInnes *et al.*, 2015) with possible implications for the contemporary production of carbonate sediments (James *et al.*, 2013), a rising sea level (McInnes *et al.*, 2015), and changes to wave climate (Hemer *et al.*, 2013; Young and Ribal, 2019).

Image quality and SfM algorithms

Alongside the relatively high scale (1:10,000 and 1:12,500) of the aerial photos which yielded GSD of less than 0.2 m, a key component of the 3D reconstruction success can probably be attributed to the high resolution scanning of the analogue photos which allowed edge recognition and subsequently positioning of objects in 3D (Gomez *et al.*, 2015; Voumard *et al.*, 2017), the quality of images (with reduced blur, darkness and haze) and the number of overlapping images (Fonstad *et al.*, 2013; Gomez *et al.*, 2015; Westoby *et al.*, 2012).

Indeed, the SfM photogrammetric software could produce a 3D surface in all attempts. However, it yielded different results when extra images were added to the initial processing stage, which probably had to do with the random seeding of the matching algorithms (Mölg and Bolch, 2017).

In theory, this limitation could be overcome if more overlapping images existed, but the reality with historical datasets is that a limited amount of overlapping images were acquired. In this sense, the option for studying beaches in Port Fairy and Warrnambool benefited from the changes in coastal orientation, as the photographic archive for the study sites clearly had additional images that were taken when the airplane was adjusting to the new coastline orientation. Therefore, the application of

the SfM method with historical photogrammetry along straight coastlines would be more limited, unless really high overlap and sidelap were planned.

The height differences between the independent points extracted from the 2007 LiDAR and the EB 1969, EB 1977 and EB 1986 DSMs, and also for the eastern part of LB 1986 DSM, highlight a couple of issues in regards to the georeferencing and construction of scene geometry in SfM, which affects the vertical quality of the final models.

Firstly, the photographic datasets were provided without much information in regards to the camera parameters. Therefore a non *priori* specification of the interior orientation was made in Pix4Dmapper, and consequently a self-calibration optimization of the bundle adjustment within the software occurred. This strategy likely led to poorly-resolving lens distortion for the near-nadir historical imagery resulting in non-linear systematic errors (James and Robson, 2014; Wackrow and Chandler, 2008; Wackrow *et al.*, 2007). Such errors were probably minimized through the use of GCPs (Eltner and Schneider, 2015), but were still apparent in the tilt of EB 1969 (Figure 7a), for instance, as identified previously by others (Stojic *et al.*, 1998; Westaway *et al.*, 2003).

Secondly, the option to use bare ground LiDAR points as GCPs seemed to be quite appropriate as the LiDAR data covered all the study area and had adequate accuracy for historical reconstruction. However, lower accuracies for selected individual points, operator's error during GCP insertion and identification of minimally disturbed areas may have introduced vertical offsets in some models.

The spatial distribution of GCPs throughout the scene, paramount to the vertical quality of DSMs (Carrivick *et al.*, 2016; Mölg and Bolch, 2017) is influenced by the identification of areas that have experienced minimal change over the years.

However, along the vegetated dune backed by the Belfast Lough on the northeastern half of EB, this has proven to be difficult, as the area has changed considerably, due to reshaping of landscape, especially dune and road opening that occurred mostly prior to 1986, and the lack of urbanisation or fixed natural objects (e.g. large and flat rock outcrops) inside the reconstructed scene. This has had an adverse effect offsetting the vertical domain of all EB models, especially for 1969 and 1977 (Figure 7a and b).

The ability of the software to spatially reconstruct the model scenes is based on the minimum overlapping requirements. This influenced not only the spatial extent of each individual models but also created non-continuous areas for EB 1977 and 1986, and also LB 1986 (Figure 3) due to poor overlap of historical photo runs. These segmented reconstructions had none to limited georeferenced points inside them and this seems to have offset the vertical domain in these segmented areas, despite the satisfactory number of GCPs used in each dataset. Absolute elevation differences for points in the second easternmost segmented area in LB 1986, have shown to be higher than in the continuous LB 1969 and LB 1977 models (Figure 3).

Elevation accuracy also gets reduced in reconstruction of historical areas surrounded by high buildings, trees and shadows, such as in some parts located to the south of the SLSC in EB 1977 and EB 1986 (Figure 3), despite the insertion of several GCPs nearby. This is clearly illustrated by the cluster of light blue dots in EB 1977 and the orange dots in EB 1986, indicating lower and higher elevation than the LiDAR-derived DSM, respectively.

Lastly, due to the ever changing natural and anthropogenic dynamics of the coast, and also the difficulty in obtaining enough historical topographic data (e.g. survey marks that haven't changed over time), SfM-derived DSMs can also produce

quite erroneous and difficult to assess topographic surfaces. RMSE values in Table III cannot clearly distinguish between systematic and random errors in the DSM models (Bakker and Lane, 2017; James *et al.*, 2019). A visual DoD comparisons (Mölg and Bolch, 2017) (Figure 4) and the skewed distribution of errors (Höhle and Höhle, 2009) (Figure 3) confirmed that some DSMs were tilted. However, accuracy measurements provided by the ME values (Table III) and the spatial distribution of errors in Figure 3 indicate the quality of the models used in volumetric calculations (Eltner *et al.*, 2016; Smith *et al.*, 2015). MAE values of less than 0.5 m (Table III) also assure the performance quality and serve as indicators of the non-directional elevation errors (Smith and Vericat, 2015; Willmott and Matsuura, 2005).

Another limitation to the application of SfM-derived DSM to build historical coastal landscapes relates to the dependence of the image matching algorithm on image texture (Fonstad *et al.*, 2013). Beaches and other highly flat and homogeneous surfaces such as sealed and unsealed roads, tend to produce poor point clouds with lots of uneven elevation pixels. Besides, the water bodies near the coast (e.g. lakes and streams) and the movement of waves during photo runs present challenges for accurate DSM reconstruction. No apparent difference was noticed between datasets based on black-and-white versus colour photographs, as also observed by Ishiguro et al. (2016).

Tide conditions reflecting on the width of the beach when photographs were taken also constitute reasons of concern in volumetric calculations. Normally, the wider the beach the more realistic chances of capturing changes are, and therefore the historical calculations have to be limited to the intersected area covered by different datasets. The water level during photogrammetric acquisition was particularly high next to the training walls (southwestern part) of EB limiting the

calculations to a 30-m wide area. This approach may have introduced biases due to detection of canopy vegetation or man-made infrastructure. Filtering superfluous topographic data via terrain derivatives, clustering and other techniques that exploit the spectral properties of the photographs (Callow *et al.*, 2018; Chehata *et al.*, 2008; Montealegre *et al.*, 2015) can possibly be used to refine volumetric calculations as long as they are able to generate a bare ground point cloud of sufficient density and accuracy.

Conclusion

This study demonstrated the potential of applying SfM photogrammetric approaches for approximate quantification of volumetric changes along sandy beaches using historical aerial images. Bare ground LiDAR data were used as GCPs at locations where topographic change over the years were minimal. Two DSMs covering the entire beach at LB in 1969 and 1977 and one covering the western half of it in 1986 were deemed of topographic quality. The DSMs of LB 1969 and LB 1977 indicated an approximate volumetric accretion of 223,000 ± 72,000 m^3 and 199,000 ± 56,000 m^3, respectively, when compared to LiDAR data acquired in 2007. Volumetric change results demonstrated the consistency of the calculations for this embayment. A much less satisfactory result was obtained for the three DSMs at EB despite the capacity of calculating erosion volumes to the east of the seawall from 1977 to 2007. Traditional shoreline analysis at both locations corroborate with patterns of volumetric accretion/erosion at both sites.

Volumetric assessments at sandy beaches were better conducted when more than one historical DSM were obtained for comparison. Successful DSMs of topographic quality were created when continuous 3D structures were produced

during the bundle adjustment phase, whereas segmented surfaces, caused by limited overlapping of images, failed to do so. Despite good indicators of dataset quality (R^2 ME and MAE of independent points), some of the DSMs were tilted as result of several issues affecting elevation. DoDs provide a good assessment of DSMs in areas where minimum change occurred and can be effective in determining poorly georeferenced sections and systematic errors in datasets. Regardless of the DSM quality, manual labour was significant to clean the point clouds due to the lack of texture in sandy environments, and no difference was noticed between black-and-white and colour photographic datasets.

Based on results of these six DSMs, several aspects of the use of SfM including strengths and weaknesses were highlighted. Volumetric calculation improvements would benefit from filtering of point clouds to transform DSMs in DEMs. The use of SfM method to archival aerial imagery can potentially serve as benchmark for erosional studies not only in Australia but throughout the world.

References

Aurecon. 2010. East Beach Coastal Erosion Engineering and Feasibility Study. Maroochydore, Australia.

Baily B, Collier P, Farres P, Inkpen R, Pearson A. 2003. Comparative assessment of analytical and digital photogrammetric methods in the construction of DEMs of geomorphological forms. *Earth Surface Processes and Landforms* **28**: 307-320. DOI: https://doi.org/10.1002/esp.481

Bakker M, Lane SN. 2017. Archival photogrammetric analysis of river-floodplain systems using Structure from Motion (SfM) methods. *Earth Surface Processes and Landforms* **42**: 1274-1286. DOI: https://doi.org/10.1002/esp.4085

Barrow J. 1854. Port Fairy. Hydrographic Office of the Admiralty: London.

Bird ECF. 1993. The coast of Victoria: the shaping of scenery. Melbourne University Press

Birdseye CH. 1940. Stereoscopic phototopographic mapping. *Annals of the Association of American Geographers* **30**: 1-24

Callow J, May S, Leopold M. 2018. Drone photogrammetry and KMeans point cloud filtering to create high resolution topographic and inundation models of coastal sediment archives. *Earth Surface Processes and Landforms* **43**: 2603-2615. DOI: http://dx.doi.org/10.1002/esp.4419

Carrivick JL, Smith MW, Quincey DJ. 2016. Structure from Motion in the Geosciences. John Wiley & Sons: West Sussex, UK

Chandler J. 1999. Effective application of automated digital photogrammetry for geomorphological research. *Earth Surface Processes and Landforms* **24**: 51-63. DOI: https://doi.org/10.1002/(SICI)1096-9837(199901)24:1<51::AID-ESP948>3.0.CO;2-H

Chehata N, David N, Bretar F. 2008. LIDAR data classification using hierarchical K-means clustering. In *ISPRS Congress Beijing 2008*. Citeseer: Beijing; 325-330.

Durrant T, Hemer M, Trenham C, Greenslade D. 2013. CAWCR Wave Hindcast 1979-2010. v8. CSIRO.

Eltner A, Kaiser A, Castillo C, Rock G, Neugirg F, Abellán A. 2016. Image-based surface reconstruction in geomorphometry – merits, limits and developments. *Earth Surf. Dynam.* **4**: 359–389. DOI: http://dx.doi.org/10.5194/esurf-4-359-2016

Eltner A, Schneider D. 2015. Analysis of different methods for 3D reconstruction of natural surfaces from parallel-axes UAV images. *The Photogrammetric Record* **30**: 279-299

Flocard F, Carley JT, Rayner DS, Rahman PF, Coghlan IR. 2013. Future Coasts- Port Fairy Coastal Hazard Assessment. WRL/UNSW: Sydney.

Fonstad MA, Dietrich JT, Courville BC, Jensen JL, Carbonneau PE. 2013. Topographic structure from motion: a new development in photogrammetric measurement. *Earth Surface Processes and Landforms* **38**: 421-430. DOI: http://dx.doi.org/10.1002/esp.3366

712 GHD. 2009. Final Report for Apollo Bay Sand and Dredging Options Study: Assessment of Sand
713 Management and Dredging Options.
714 Gill ED. 1967. Evolution of the Warrnambool-Port Fairy coast and the Tower Hill eruption, western
715 Victoria. In *Landform Studies from Australia and New Guinea*; 340-364.
716 Gill ED. 1984. Coastal Processes and the Sanding of Warrnambool Harbour: Definition of Coastal
717 Processes, Quantification of Sand Erosion/deposition and the Reason for the Sanding Up of the
718 Harbour at Warrnambool, SW Victoria, Australia. Warrnambool Institute Press
719 Gomez C, Hayakawa Y, Obanawa H. 2015. A study of Japanese landscapes using structure from
720 motion derived DSMs and DEMs based on historical aerial photographs: New opportunities for
721 vegetation monitoring and diachronic geomorphology. *Geomorphology* **242**: 11-20. DOI:
722 http://dx.doi.org/10.1016/j.geomorph.2015.02.021
723 Grip WM, Grip RW, Morrison RD. 2000. Application of aerial photography and photogrammetry in
724 environmental forensic investigations. *J Environmental Forensics* **1**: 121-129. DOI:
725 http://dx.doi.org/10.1006/enfo.2000.0014
726 Harris PT, Hughes MG. 2012. Predicted benthic disturbance regimes on the Australian continental
727 shelf: a modelling approach. *Marine Ecology Progress Series* **449**: 13-25. DOI:
728 http://dx.doi.org/10.3354/meps09463
729 Hemer MA, Fan Y, Mori N, Semedo A, Wang XL. 2013. Projected changes in wave climate from a
730 multi-model ensemble. *Nature Climate Change* **3**: 471-476. DOI:
731 http://dx.doi.org/10.1038/NCLIMATE1791
732 Himmelstoss EA, Henderson RE, Kratzmann MG, Farris AS. 2018. Digital Shoreline Analysis System
733 (DSAS) version 5.0 user guide. U.S. Geological Survey; 110.
734 Höhle J, Höhle M. 2009. Accuracy assessment of digital elevation models by means of robust
735 statistical methods. *ISPRS Journal of Photogrammetry and Remote Sensing* **64**: 398-406. DOI:
736 http://dx.doi.org/10.1016/j.isprsjprs.2009.02.003

737 Ierodiaconou D, Schimel AC, Kennedy DM. 2016. A new perspective of storm bite on sandy beaches
738 using unmanned aerial vehicles. *Zeitschrift fur Geomorphologie* **60**: 123-137. DOI:
739 http://dx.doi.org/10.1127/zfg_suppl/2016/00247
740 Ishiguro S, Yamano H, Oguma H. 2016. Evaluation of DSMs generated from multi-temporal aerial
741 photographs using emerging structure from motion–multi-view stereo technology. *Geomorphology*
742 **268**: 64-71. DOI: http://dx.doi.org/10.1016/j.geomorph.2016.05.029
743 James MR, Chandler JH, Eltner A, Fraser C, E. Miller P, Mills JP, Noble T, Robson S, Lane SN. 2019.
744 Guidelines on the use of structure-from-motion photogrammetry in geomorphic research. *Earth*
745 *Surface Processes and Landforms* **44**: 2081–2084. DOI: http://dx.doi.org/10.1002/esp.4637
746 James MR, Robson S. 2012. Straightforward reconstruction of 3D surfaces and topography with a
747 camera: Accuracy and geoscience application. *Journal of Geophysical Research: Earth Surface* **117**: 1-
748 17. DOI: http://dx.doi.org/10.1029/2011jf002289
749 James MR, Robson S. 2014. Mitigating systematic error in topographic models derived from UAV and
750 ground-based image networks. *Earth Surface Processes and Landforms* **39**: 1413-1420. DOI:
751 http://dx.doi.org/10.1002/esp.3609
752 James NP, Reid CM, Bone Y, Levings A, Malcolm I. 2013. The macroalgal carbonate factory at a cool-
753 to-warm temperate marine transition, southern Australia. *Sedimentary Geology* **291**: 1-26
754 Konlechner TM, Kennedy DM, Cousens RD, Woods JLD. 2019. Patterns of early-colonising species on
755 eroding to prograding coasts; implications for foredune plant communities on retreating coastlines.
756 *Geomorphology* **327**: 404-416. DOI: https://doi.org/10.1016/j.geomorph.2018.11.013
757 Kraus NC, McDougal WG. 1996. The effects of seawalls on the beach: Part I, an updated literature
758 review. *Journal of Coastal Research* **12**: 691-701
759 Lane S, Widdison P, Thomas R, Ashworth P, Best JL, Lunt I, Sambrook Smith G, Simpson C. 2010.
760 Quantification of braided river channel change using archival digital image analysis. *Earth Surface*
761 *Processes and Landforms* **35**: 971-985. DOI: http://dx.doi.org/10.1002/esp.2015

762 Lowe DG. 2004. Distinctive image features from scale-invariant keypoints. *International journal of*
763 *computer vision* **60**: 91-110
764 McInnes K, Monselesan D, Church J, Lenton A, J. OG. 2015. Projections (and recent trends): Marine
765 and Coasts. In *Climate Change in Australia Information for Australia's Natural Resource Management*
766 *Regions: Technical Report*. CSIRO/Bureau of Meteorology: Australia.
767 McLean R, Shen J-S. 2006. From foreshore to foredune: Foredune development over the last 30
768 years at Moruya Beach, New South Wales, Australia. *Journal of Coastal Research*: 28-36
769 Miles D. 2019. Port Fairy's decades-long push for wall to stop seaside tip spewing rubbish into the
770 ocean to rise from the waves. In *ABC News*. ABC South West Victoria:
771 https://www.abc.net.au/news/2019-05-31/port-fairy-takes-steps-to-fix-old-tip-site/11159736.
772 Mölg N, Bolch T. 2017. Structure-from-Motion Using Historical Aerial Images to Analyse Changes in
773 Glacier Surface Elevation. *Remote Sensing* **9**. DOI: http://dx.doi.org/10.3390/rs9101021
774 Montealegre AL, Lamelas MT, de la Riva J. 2015. A comparison of open-source LiDAR filtering
775 algorithms in a Mediterranean forest environment. *IEEE Journal of Selected Topics in Applied Earth*
776 *Observations and Remote Sensing* **8**: 4072-4085. DOI:
777 http://dx.doi.org/10.1109/JSTARS.2015.2436974
778 Neal M. 2012. Urgent works to dredge Lady Bay. In *The Standard*: Warrnambool.
779 Nebiker S, Lack N, Deuber M. 2014. Building change detection from historical aerial photographs
780 using dense image matching and object-based image analysis. *Remote Sensing* **6**: 8310-8336. DOI:
781 https://doi.org/10.3390/rs6098310
782 Ollier CD. 1985. Lava flows of Mount Rouse, western Victoria. *Proceedings of the Royal Society of*
783 *Victoria* **97**: 167-174
784 Plant NG, Griggs GB. 1992. Interactions between nearshore processes and beach morphology near a
785 seawall. *Journal of Coastal Research* **8**: 183-200

Porter-Smith R, Harris P, Andersen O, Coleman R, Greenslade D, Jenkins C. 2004. Classification of the Australian continental shelf based on predicted sediment threshold exceedance from tidal currents and swell waves. *Marine Geology* **211**: 1-20. DOI: http://dx.doi.org/10.1016/j.margeo.2004.05.031

Schenk T. 2005. Introduction to Photogrammetry. The Ohio State University: Columbus

Schimel AC, Ierodiaconou D, Hulands L, Kennedy DM. 2015. Accounting for uncertainty in volumes of seabed change measured with repeat multibeam sonar surveys. *Continental Shelf Research* **111**: 52-68. DOI: http://dx.doi.org/10.1016/j.csr.2015.10.019

Seccaroni S, Santangelo M, Marchesini I, Mondini AC, Cardinali M. 2018. Highresolution historical topography: getting more from archival aerial photographs. In *2nd International Electronic Conference on Remote Sensing (ECRS 2018)*. Sciforum Electronic Conference Series.

Short AD. 1996. Beaches of the Victorian Coast & Port Phillip Bay: A Guide to Their Nature, Characteristics, Surf and Safety. Sydney University Press

Smith MW, Carrivick JL, Quincey DJ. 2015. Structure from motion photogrammetry in physical geography. *Progress in Physical Geography* **40**: 247-275. DOI: http://dx.doi.org/10.1177/0309133315615805

Smith MW, Vericat D. 2015. From experimental plots to experimental landscapes: topography, erosion and deposition in sub-humid badlands from Structure-from-Motion photogrammetry. *Earth Surface Processes and Landforms* **40**: 1656–1671. DOI: http://dx.doi.org/10.1002/esp.3747

Snavely N. 2008. Scene reconstruction and visualization from Internet photo collections. University of Washington: USA.

Snavely N, Seitz SM, Szeliski R. 2008. Modeling the world from internet photo collections. *International journal of computer vision* **80**: 189-210. DOI: https://doi.org/10.1007/s11263-007-0107-3

Stanley HJ. 1870. Port Fairy. Hydrographic Office: London.

Stojic M, Chandler J, Ashmore P, Luce J. 1998. The assessment of sediment transport rates by automated digital photogrammetry. *Photogrammetric Engineering Remote Sensing* **64**: 387-395

812 Thom B, Hall W. 1991. Behaviour of beach profiles during accretion and erosion dominated periods.
813 *Earth Surface Processes and Landforms* **16**: 113-127
814 Triggs B, McLauchlan PF, Hartley RI, Fitzgibbon AW. 1999. Bundle adjustment—a modern synthesis.
815 In *Vision Algorithms '99*, Triggs B, Zisserman A, Szeliski R (eds). Springer-Verlag: Berlin Heidelberg;
816 298-372.
817 Turner IL, Harley MD, Short AD, Simmons JA, Bracs MA, Phillips MS, Splinter KD. 2016. A multi-
818 decade dataset of monthly beach profile surveys and inshore wave forcing at Narrabeen, Australia.
819 *Scientific data* **3**: 160024
820 Voumard J, Abellán A, Nicolet P, Penna I, Chanut M-A, Derron M-H, Jaboyedoff M. 2017. Using street
821 view imagery for 3-D survey of rock slope failures. *Natural Hazards Earth System Sciences* **17**: 2093-
822 2107. DOI: http://dx.doi.org/10.5194/nhess-17-2093-2017
823 Wackrow R, Chandler JH. 2008. A convergent image configuration for DEM extraction that minimises
824 the systematic effects caused by an inaccurate lens model. *The Photogrammetric Record* **23**: 6-18.
825 DOI: https://doi.org/10.1111/j.1477-9730.2008.00467.x
826 Wackrow R, Chandler JH, Bryan P. 2007. Geometric consistency and stability of consumer-grade
827 digital cameras for accurate spatial measurement. *The Photogrammetric Record* **22**: 121-134. DOI:
828 https://doi.org/10.1111/j.1477-9730.2007.00436.x
829 Water Technology. 2012. Port of Warrnambool: safer boating and harbour facility study.
830 WBM. 2007. Port Fairy East Beach Coastal Erosion Engineering and Feasibility Study.
831 WCC. 2019. Dredging at the Port of Warrnambool.
832 Westaway R, Lane S, Hicks D. 2003. Remote survey of large-scale braided, gravel-bed rivers using
833 digital photogrammetry and image analysis. *International Journal of Remote Sensing* **24**: 795-815.
834 DOI: http://dx.doi.org/10.1080/01431160110113070
835 Westoby MJ, Brasington J, Glasser NF, Hambrey MJ, Reynolds JM. 2012. 'Structure-from-Motion'
836 photogrammetry: A low-cost, effective tool for geoscience applications. *Geomorphology* **179**: 300-
837 314. DOI: https://doi.org/10.1016/j.geomorph.2012.08.021

Wheaton JM, Brasington J, Darby SE, Sear DA. 2010. Accounting for uncertainty in DEMs from repeat topographic surveys: improved sediment budgets. *Earth Surface Processes and Landforms* **35**: 136-156. DOI: https://doi.org/10.1002/esp.1886

Willmott CJ, Matsuura K. 2005. Advantages of the mean absolute error (MAE) over the root mean square error (RMSE) in assessing average model performance. *Climate Research* **30**: 79-82

Young IR, Ribal A. 2019. Multiplatform evaluation of global trends in wind speed and wave height. *Science* **365**: 548-552. DOI: http://dx.doi.org/10.1126/science.aav9527

Acknowledgements

Research funds for this project, as well as aerial imagery was provided by the Victorian Department of Environment, Land, Water and Planning as part of the Victorian Coastal Monitoring Program (VCMP) supported by the Sustainability Fund, Deakin University and the University of Melbourne. We thank Blake Allan for support while processing data in Pix4D, and the assessments provided by the anonymous reviewers and editors which improved the manuscript.

Conflict of Interest

The authors declare that there is no conflict of interest that could be perceived as prejudicing the impartiality of the research reported

Data availability

862 The data sets used and/or analyzed during the current study are available from the
863 corresponding author on reasonable request.
864

Figure 1. Study sites along the southwest coast of Victoria, Australia (a). Hatched polygons indicate Mount Rouse lava flow. East Beach in Port Fairy (b) and Lady Bay in Warrnambool (c).

Figure 2. Processing workflow to calculate beach volumetric change based on LiDAR-derived DSM and SfM-derived DSMs from historical archive, and shoreline analysis at each study site.

Figure 3. Area covered by each historical DSM for Lady Bay (top) and East Beach (bottom), location of GCP (green crossed dots) and independent points used in accuracy assessments for each model. Coloured dots refer to elevation difference (m) between LiDAR independent points used in accuracy assessments and SfM-derived DSMs. Negative values (hot colours) represent higher elevation in DSMs, whereas positive values (cold colours) represent lower elevation than LiDAR accuracy points. The coefficient of determination (R^2) and the frequency (*y*-axis = 75) distribution of errors (Δh = 4 m) are included for model comparisons.

Figure 4. Historical DSM generated for Lady Bay (top) and East Beach (bottom) in 1969, 1977, 1986 derived from SfM. A 2007 LiDAR-derived DSM for both sites is shown on the right for comparison. For visualisation purpose, only the beach and backdune parts of the DSMs are shown.

Figure 5. Oblique views near the SLSC at Lady Bay in 1969 (a), 1977 (b) and 1986 (c), and elevation profiles over time extracted from different Lady Bay datasets (d).

889 Oblique views centred at the present-day end of the seawall at East Beach before
890 the extension in 1977 (e) and after the extension in1986 (f).
891
892 **Figure 6.** DoDs (m) between 2007 LiDAR-derived DSM and 1969 (a), 1977 (b) and
893 1986 (c) SfM-derived DSMs for Lady Bay. Red pixels (negative values) indicate
894 areas of erosion, whereas blue pixels (positive values) indicate areas where
895 deposition occurred. An absolute value of 0.5 m was used to represent areas of no
896 change (yellow pixels). Note the elevation offset in the eastern segmented parts of
897 2007-1986 (c), excluded from volumetric analysis. Volumetric change from eastern
898 bound (breakwater) calculated using 100-m spaced shore-perpendicular transects
899 (d). Negative values in X axis indicate erosion, whereas positive values indicate
900 deposition. Zoomed-in sector in LB 2007-1986 (c) shows erosion-deposition
901 transitional area on the beach.
902
903 **Figure 7.** DoDs (m) between 2007 LiDAR-derived DSM and 1969 (a), 1977 (b) and
904 1986 (c) SfM-derived DSMs for East Beach. Red pixels (negative values) indicate
905 areas where erosion happened, whereas blue pixels (positive values) indicate areas
906 where deposition occurred. An absolute value of 0.5 m was used to represent areas
907 of no change (yellow pixels). Note the elevation offset in 2007-1969 (a), 2007-1986
908 (c) and the segmented northeastern and southwestern areas in 2007-1977 (b),
909 excluded from volumetric analysis. Volumetric change from southeastern bound
910 (training walls) calculated using 100-m spaced shore-perpendicular transects (d).
911 Negative values in X axis indicate erosion, whereas positive values indicate
912 deposition. Zoomed-in sector in EB 2007-1977 (b) shows heavy erosion to the
913 northeast of the seawall.

Figure 8. Shoreline analysis at Lady Bay based on digitised vegetation shoreline positions (a). Linear regression rate (LRR) (b) and shoreline change envelope (SCE) (c) at 10-m spaced transects from 1969 to 2007. Net shoreline movement (NSM) at each transect between 1969 and 2007 (d), 1977 and 2007 (e) and 1986 and 2007 (f). Zoomed-in sectors in (a) and (b) show shoreline transitional retreat-propagation zone approximately 500 m to the north of the breakwater, as determined by shoreline positions and 10-m spaced transects, respectively.

Figure 9. Shoreline analysis at East Beach based on digitised vegetation shoreline positions (a). Linear regression rate (LRR) (b) and shoreline change envelope (SCE) (c) at 10-m spaced transects from 1969 to 2007. Net shoreline movement (NSM) at each transect between 1969 and 2007 (d), 1977 and 2007 (e) and 1986 and 2007 (f). Zoomed-in sectors in (a) and (b) show shoreline retreat and highest LRR as determined by 10-m spaced transects, respectively, to the northeast of the seawall.

Table I: Aerial photograph characteristics used in the SfM processing of DSMs.

Site	Date	Scale	Camera	Height	Run	# Photos	Type
LB	27-Dec-69	1:12,500	RC8	6,100	3, 4, 5, 9 & 10	17	B/W
LB	11-Feb-77	1:10,000	RC8	5,000	21, 22 & 23	11	B/W
LB	1-Apr-86	1:10,000	RC10	10,000	17 & 18	10	Colour
EB	9-Dec-69	1:12,500	RC8	6,000	1, 2 & 3	15	B/W
EB	11-Feb-77	1:10,000	RC8	5,000	24, 25 & 26	14	B/W
EB	1-Apr-86	1:10,000	RC10	10,000	14, 15 &16	18	Colour

Table II. Spatial extent of SfM-derived DSMs, ground sampling distance (GSD), ground control points (GCPs) and image processing parameters.

Dataset	SfM area (km^2)	GSD (cm)	Number of GCP	Average keypoints/image	Camera optimisation (%)	Average matches/ calibrated images	Georeferencing RMSE (m)
LB 1969	11.5	18.6	23	86,025	15.4	13,789	0.92
LB 1977	6.4	15.9	21	53,381	13.8	14,015	0.89
LB 1986	5	15.4	15	73,580	62.3	23,652	0.52
EB 1969	13.8	18.1	16	65,073	0.6	17,040	0.98
EB 1977	8.8	16.1	16	53,155	6.3	14,357	0.77
EB 1986	8.3	15.4	22	64,098	28.7	21,100	0.62

Table III. Summary of errors using independent points to validate SfM-DSMs

Dataset	R^2	RMSE (m)	ME (m)	SDE (m)	MAE (m)
LB 1969	0.99 (n=141)	0.63	-0.46	0.44	0.49
LB 1977	0.99 (n=94)	0.50	-0.03	0.51	0.38
LB 1986	0.99 (n=81)	0.58	-0.19	0.55	0.45
EB 1969	0.92 (n=78)	0.99	-0.57	0.81	0.7
EB 1977	0.96 (n=107)	0.62	0.62	0.62	0.48
EB 1986	0.84 (n=119)	0.91	0.04	0.92	0.68

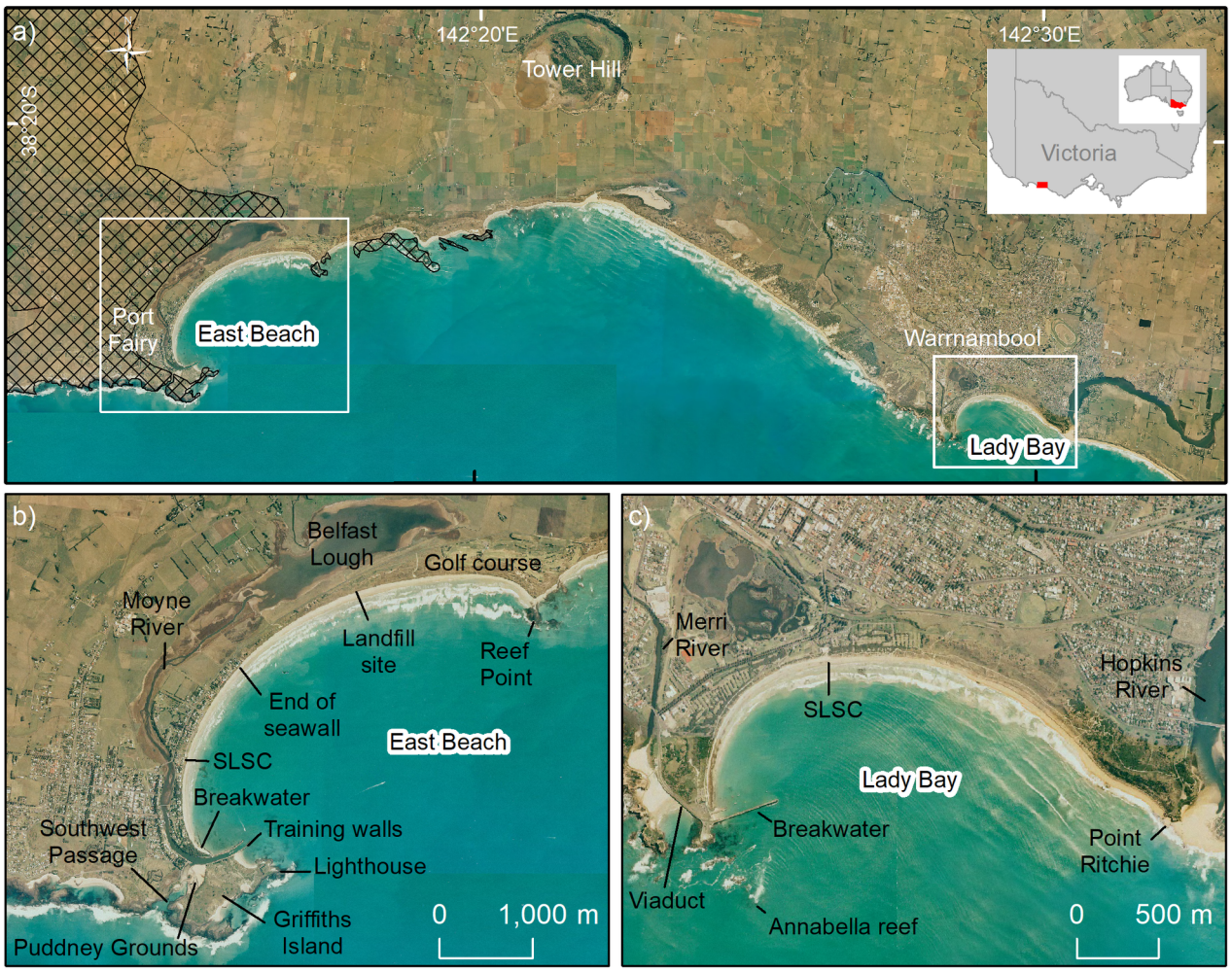

ESP_4911_F1.tif

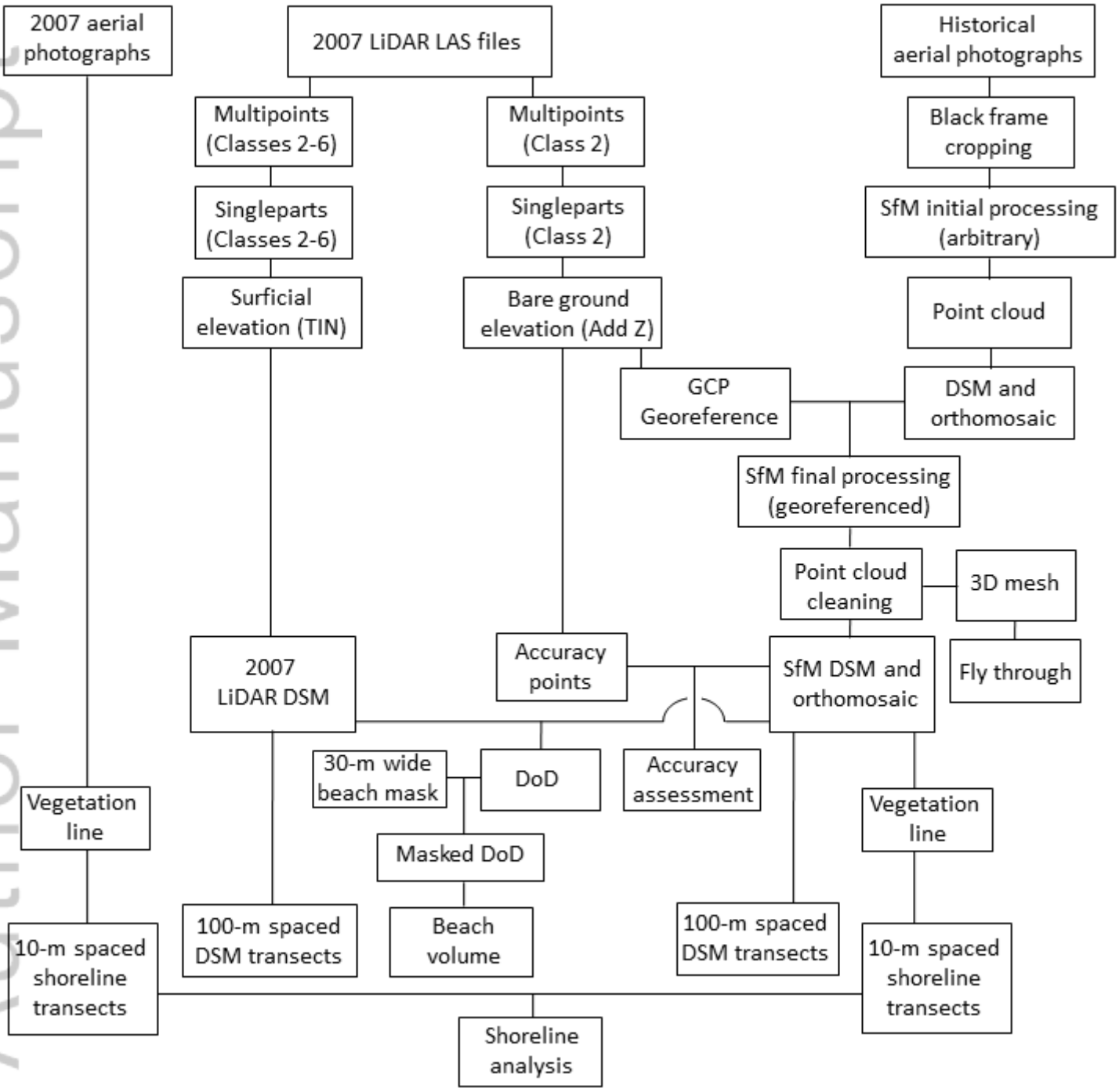

ESP_4911_F2.tif

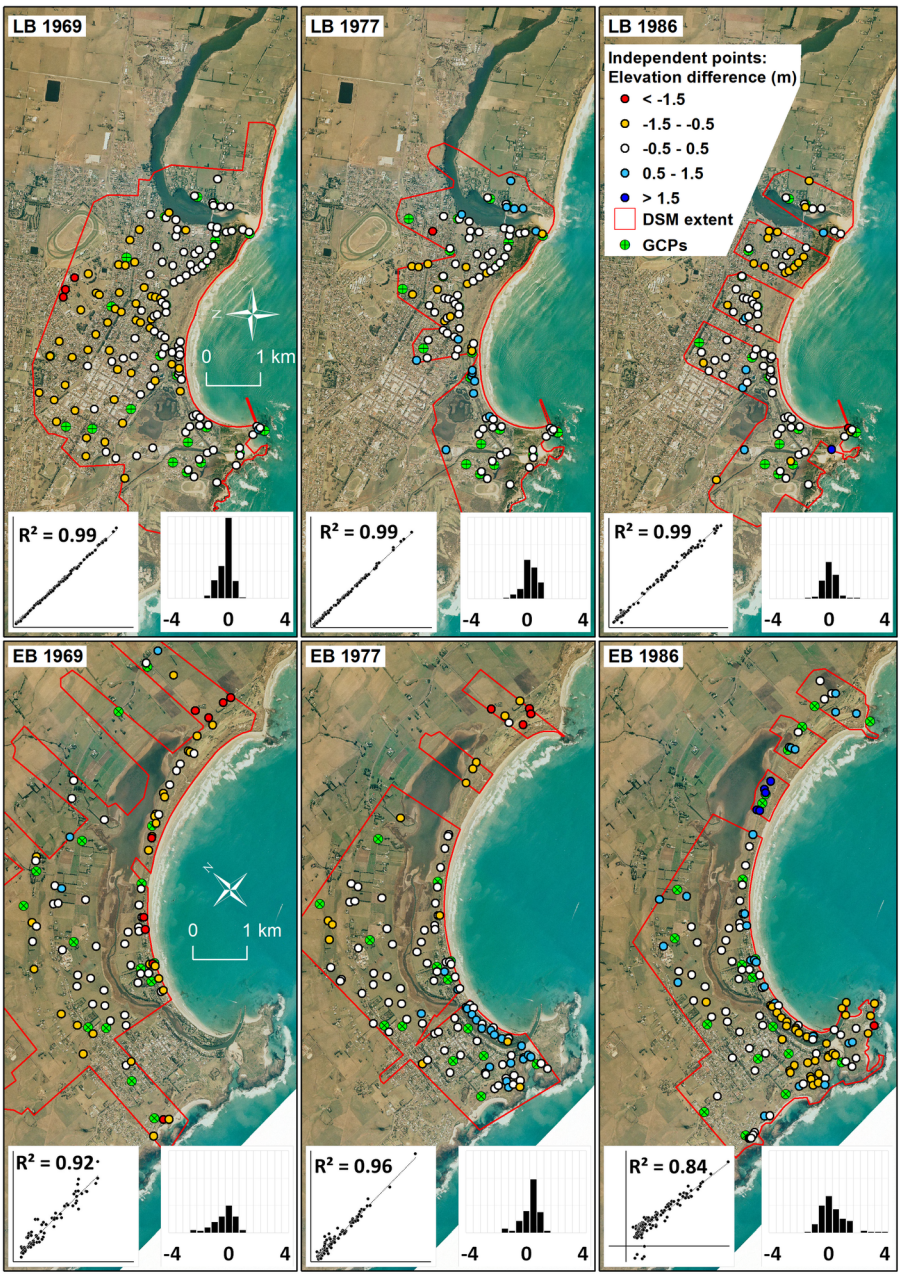

ESP_4911_F3.tif

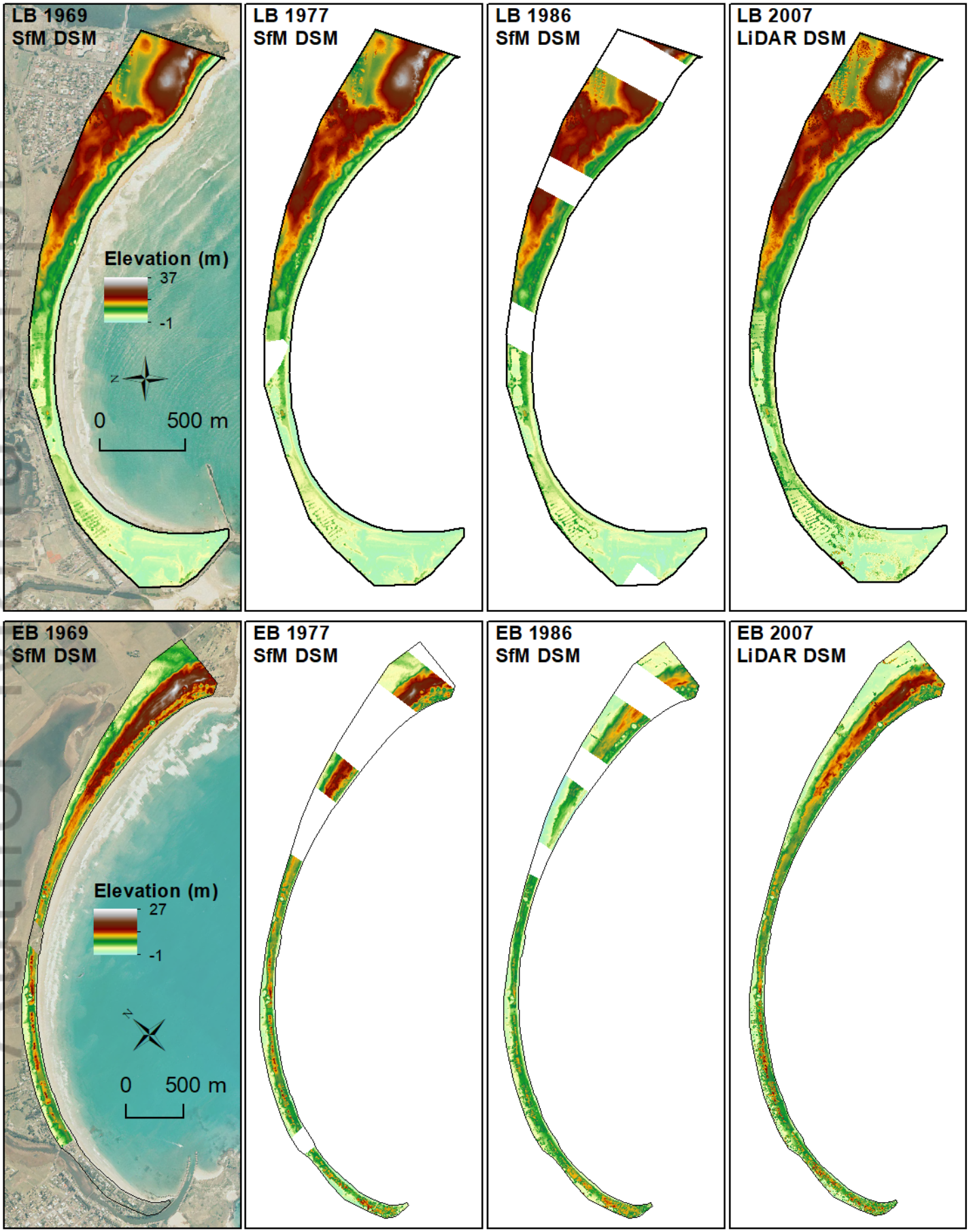

ESP_4911_F4.tif

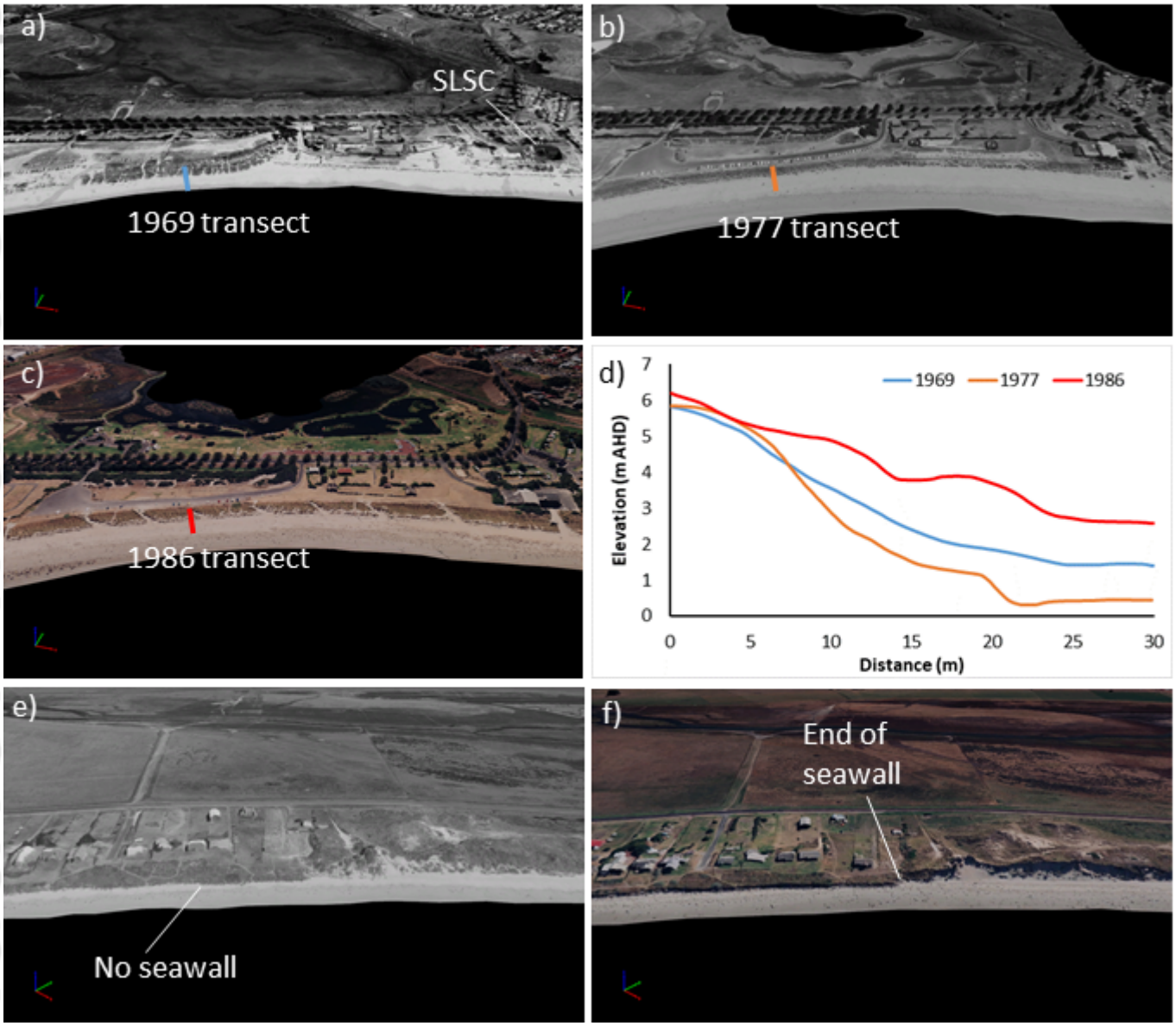

ESP_4911_F5.tif

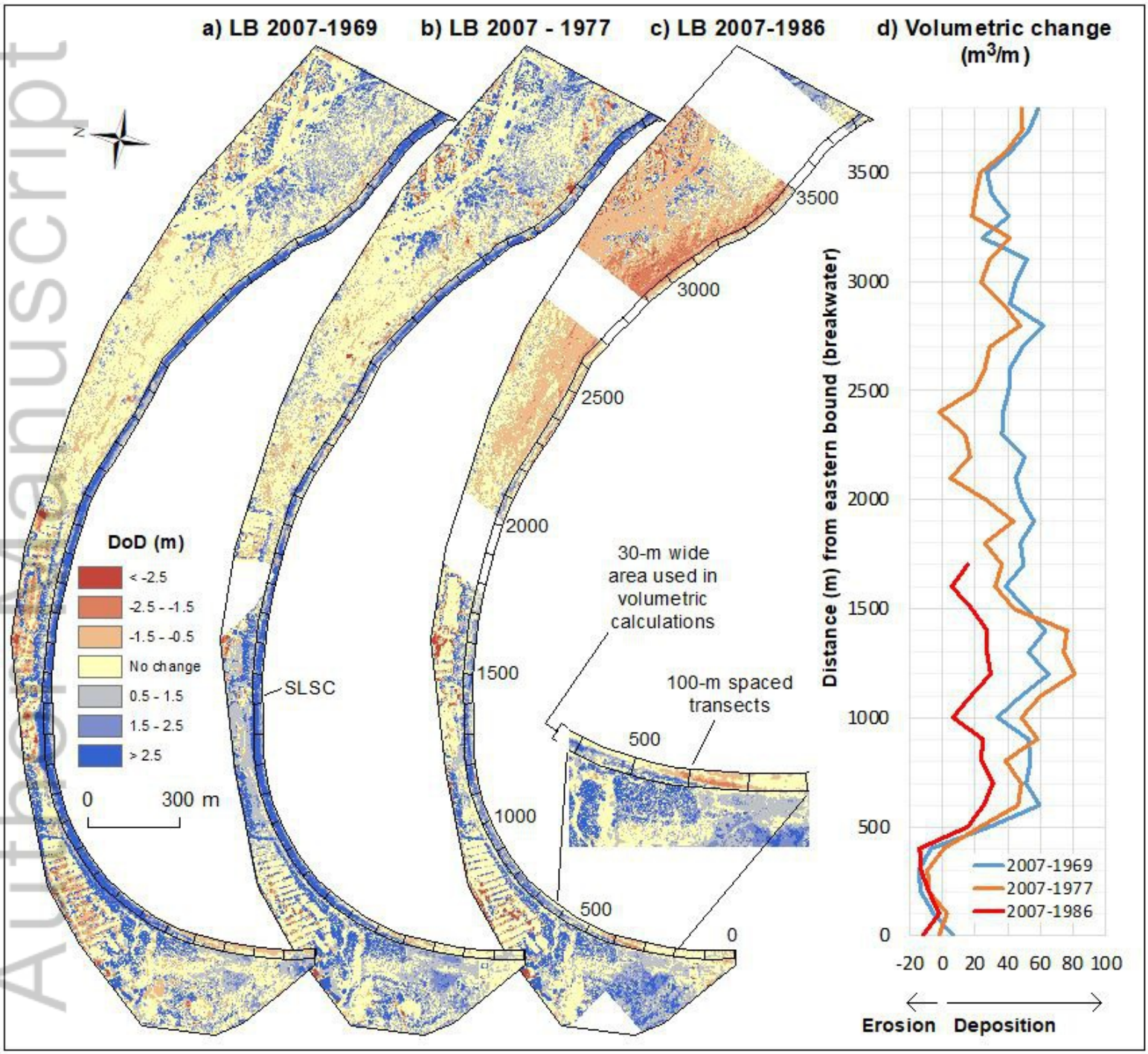

ESP_4911_F6.JPG

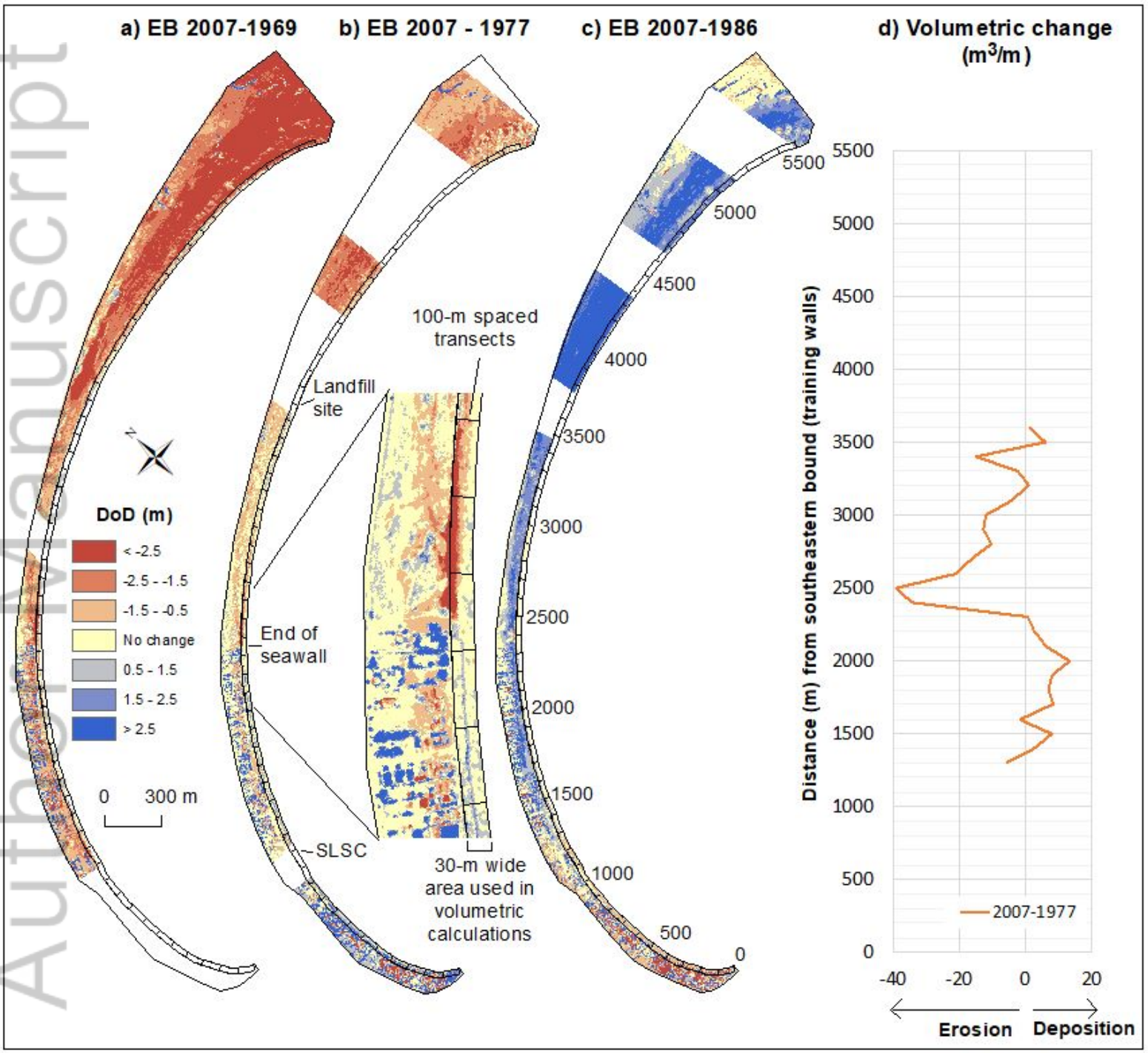

ESP_4911_F7.tif

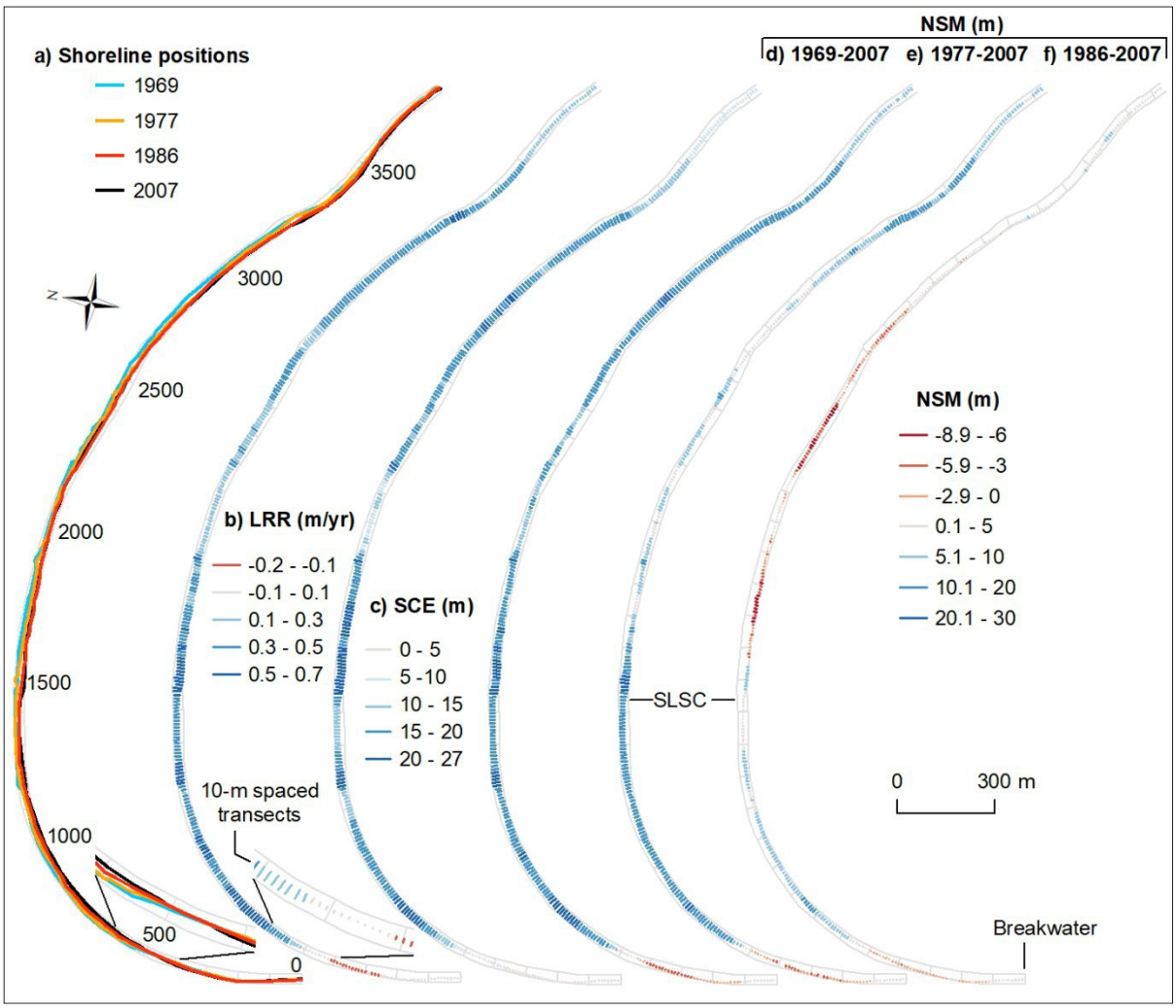

ESP_4911_F8.jpg

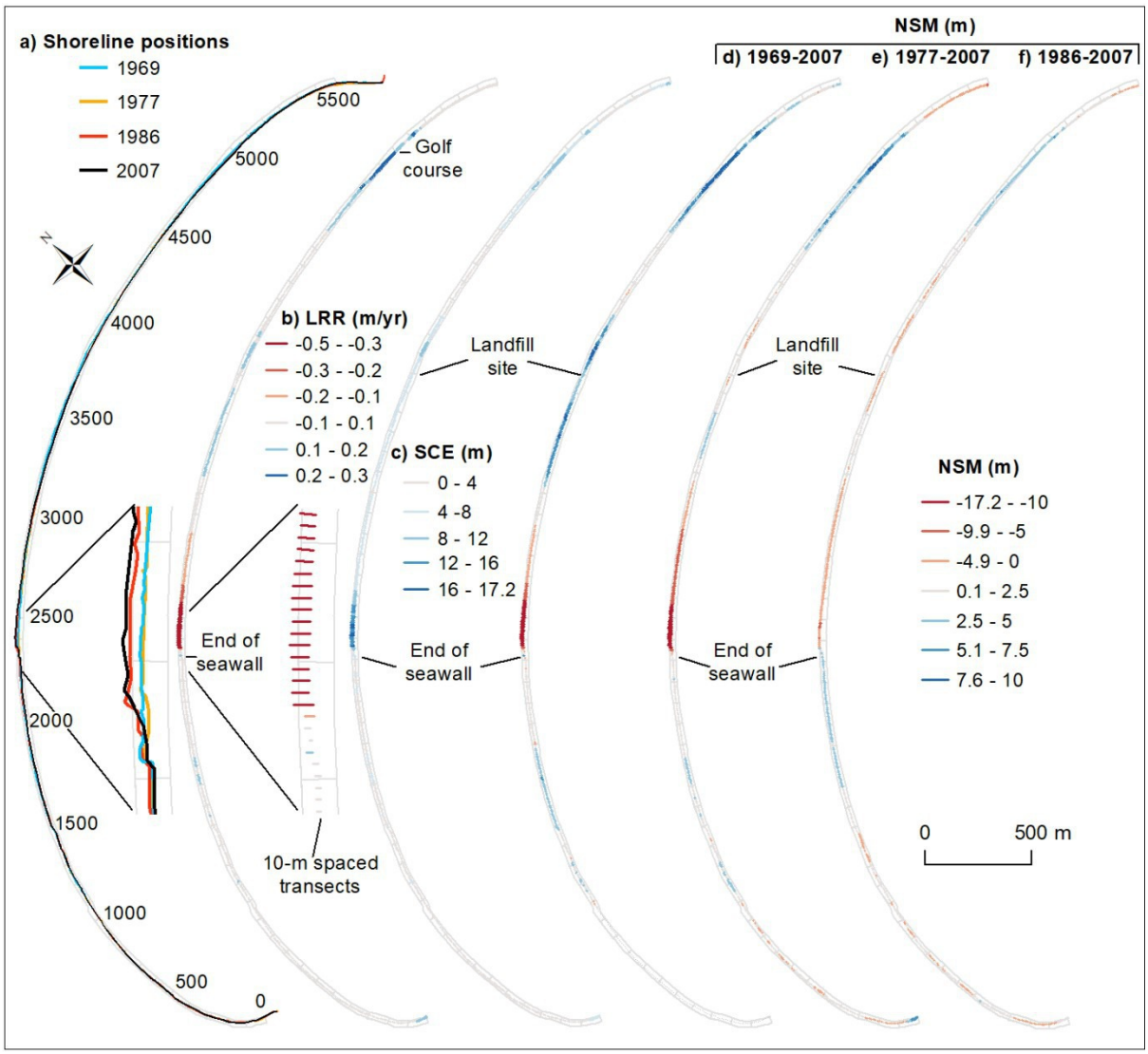

ESP_4911_F9.jpg